Computer-Aided Civil and Infrastructure Engineering **18** (2003) 339–355

Wavelet Transforms for System Identification in Civil Engineering

T. Kijewski & A. Kareem*

NatHaz Modeling Laboratory, Department of Civil Engineering and Geological Sciences, University of Notre Dame, Notre Dame, IN 46556, USA

Abstract: *The time-frequency character of wavelet transforms allows adaptation of both traditional time and frequency domain system identification approaches to examine nonlinear and non-stationary data. Although challenges did not surface in prior applications concerned with mechanical systems, which are characterized by higher frequency and broader-band signals, the transition to the time-frequency domain for the analysis of civil engineering structures highlighted the need to understand more fully various processing concerns, particularly for the popular Morlet wavelet. In particular, as these systems may possess longer period motions and thus require finer frequency resolutions, the particular impacts of end effects become increasingly apparent. This study discusses these considerations in the context of the wavelet's multiresolution character and includes guidelines for selection of wavelet central frequencies, highlights their role in complete modal separation, and quantifies their contributions to end-effect errors, which may be minimized through a simple padding scheme.*

1 INTRODUCTION

While the Fourier transform has reshaped the way in which engineers interpret signals, it becomes evident that by breaking a signal into a series of trigonometric basis functions, time-varying features cannot be captured. Thus, basic signal analysis or system identification may be potentially hindered by this limitation. The realization that non-stationary features characterize many processes of interest led to the definition of alternative transforms that rely on bases with compact support. As Fourier basis functions are localized in frequency but not in time, one alternative was introduced by Gabor to localize the Fourier transform through the short time Fourier transform (STFT). However, the constraints of the Heisenberg uncertainty principle limit the obtainable resolutions considerably, prompting an alternative approach to time-frequency analysis, featuring basis functions that have compact support in both frequency and time to yield a multi-resolution analysis termed the wavelet transform (Carmona et al., 1998; Chui, 1992).

*To whom correspondence should be addressed. E-mail: *kareem@nd.edu*.

1.1 Governing relationships

The wavelet transform is a linear transform, which decomposes a signal $x(t)$ via basis functions that are simply dilations and translations of the parent wavelet $g(t)$ through the convolution of the signal and the scaled parent wavelet according to

$$W(a,t) = \frac{1}{\sqrt{a}} \int_{-\infty}^{\infty} x(\tau) g^* \left(\frac{t-\tau}{a} \right) d\tau \qquad (1)$$

Dilation by the scale, a, inversely proportional to frequency, represents the periodic or harmonic nature of the signal. By this approach, time-frequency localization is possible, since the parent wavelet serves as a "window function," as opposed to the trigonometric bases of the Fourier transform. The wavelet coefficients, $W(a,t)$, represent a measure of the similitude between the dilated/shifted parent wavelet and the signal at that time t and scale (frequency) a.

Though there are countless parent wavelets used in practice, of both discrete and continuous form, this article shall focus on the continuous wavelet transform (CWT) using the Morlet wavelet (Grossman and Morlet, 1990), as its analogs to the Fourier transform make it

quite attractive for harmonic analysis. These analogs are evident from the Morlet basis function

$$g(t) = e^{i\omega_o t} e^{-t^2/2} = e^{-t^2/2} (\cos(\omega_o t) + i \sin(\omega_o t)) \quad (2)$$

Essentially, the Morlet wavelet in Equation (2) is a Gaussian-windowed Fourier transform, with sines and cosines oscillating at the central frequency, $f_o(\omega_o = 2\pi f_o)$. Dilations of this temporally localized parent wavelet then allow the "effective frequency" of this sine-cosine pair to change so as to match harmonic components within the signal. The Morlet wavelet is equivalently localized in the frequency domain, as evidenced by the Fourier transform of the dilated Morlet wavelet

$$G(af) = \sqrt{2}\sqrt{\pi} e^{-2\pi^2 (af - f_o)^2} \quad (3)$$

For the Morlet wavelet, there is a unique relationship between the dilation parameter of the transform, a, and the Fourier frequency, f, at which the wavelet is focused. This relationship is evident by maximizing Equation (3) to yield

$$a = f_o / f \quad (4)$$

1.2 Wavelets in system identification

The Morlet wavelet and other classes of discrete and continuous wavelets have been applied to a variety of problems ranging from image and acoustic processing to fractal analysis. Recently, the analysis of stochastic processes of interest to civil engineering adapted wavelets to a number of situations where Fourier transforms were traditionally used to define quantities of interest, for example, for estimates of auto and cross-spectra (Gurley and Kareem, 1999).

Meanwhile, the more rigorous application of wavelets to system identification of mechanical systems is still advancing, but shows great promise thanks to the expanse of parent wavelets available and flexibility inherent in the wavelet transform itself. This flexibility is conceptualized in Figure 1 for a simple harmonic signal. The squared modulus of the wavelet transform, or *scalogram*, is shown three dimensionally in the time-frequency domain. As discussed in greater detail in Carmona et al. (1998), the wavelet coefficients take on maximum values at the *instantaneous frequency*, corresponding to dominant frequency components in the signal at each instant in time. These define *ridges* in the time-frequency plane. Extracting the values of the wavelet coefficients along each ridge yields a wavelet *skeleton*, whose real and imaginary components approximate the signal and its Hilbert transform at that ridge frequency (see left inset of Figure 1). A time-domain-based system identification scheme using the amplitude and phase of the analytic signal can then take advantage of these skeleton components; see, for example, Staszewski (1997, 1998) and Ruzzene et al. (1997). Similarly, a slice of the

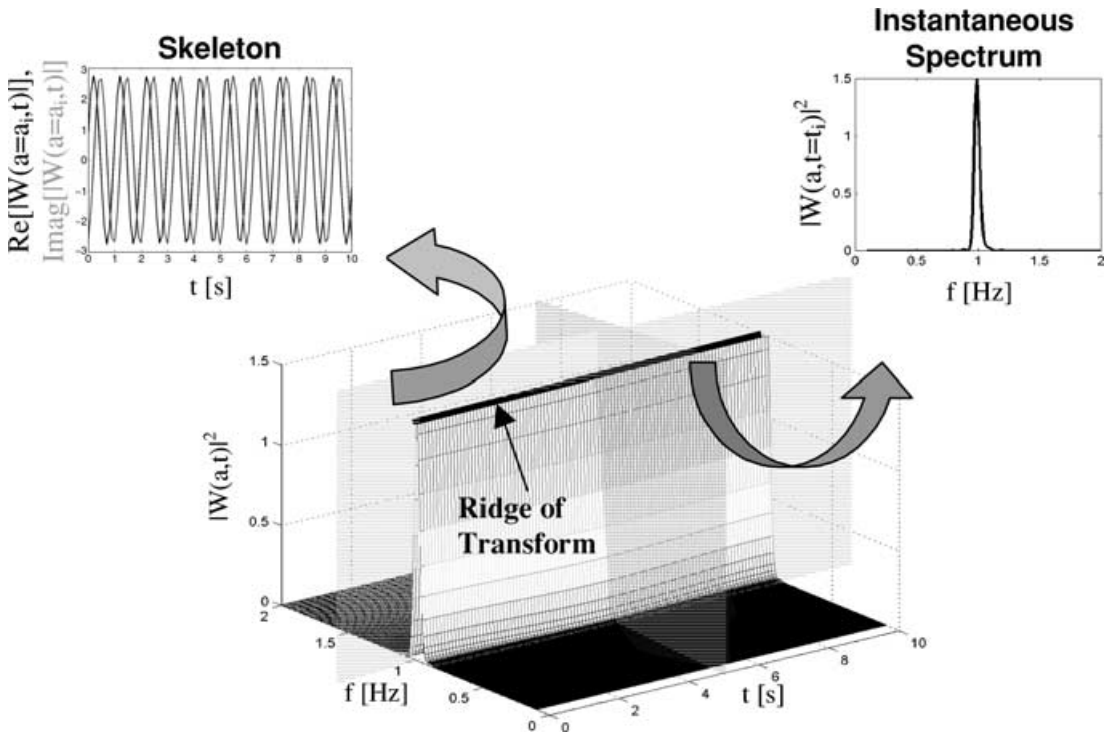

Fig. 1. Wavelet time-frequency system identification concept.

scalogram at a given time, across the range of frequencies, yields the *instantaneous spectrum* of the signal (see right inset of Figure 1), indicating the frequency content at that instant in time. Much like the Fourier spectra, the peak of this spectrum corresponds to the instantaneous frequency defining the ridge and the bandwidth of the spectrum provides an indication of the spread of frequencies present in the signal at each instant in time. This spectral information can be utilized in more traditional frameworks for system identification via frequency response functions (Hartin, 2001; Staszewski and Giacomin, 1997), for coherence analysis (Gurley et al., 2003) and for general time-frequency signal analysis (Kijewski and Kareem, 2002a).

A number of researchers have noted this dual identification potential, integrating the wavelet transform with number of system identification schemes traditionally based on Fourier transforms, for example, Coca and Billings (1997), Robertson et al. (1998a,b), Ghanem and Romeo (2000); however, when some of these approaches are introduced in civil engineering, where structures are characterized by more narrowbanded responses than most mechanical systems, certain processing concerns emerge. As these systems are usually of longer period, frequency resolutions must be refined to insure modal separation. This in turn results in an increase of end-effect errors that can have a dramatic influence on the quality of wavelet amplitudes and modal properties such as damping. The occurrence of these phenomena is rationalized in this study for the popular Morlet wavelet, guidelines for selection of critical parameters are provided, and a padding scheme to minimize end effects is introduced. Demonstrations on simulated and measured full-scale data highlight these important considerations, as wavelet-based system identification schemes are adapted to civil engineering applications.

2 WAVELET RESOLUTIONS

Though a host of time-frequency transformations are available, only the wavelet transform is uniquely capable of adaptively adjusting to the Heisenberg uncertainty principle. In essence, the wavelet transform concedes that arbitrarily good resolution in both time and frequency is not possible. Thus the transform optimizes its resolutions as needed. It provides good resolution at high dilations or low frequencies, ideal for civil engineering applications, while sacrificing its time resolution in this regime to satisfy the uncertainty principle. In the time domain, the transform has good resolution at high frequencies so as to identify signal singularities or discontinuities, a feature often exploited in health monitoring applications; see, for example, Corbin et al. (2000).

The time (Δt) and frequency (Δf) resolutions of the wavelet transform are given by (Chui, 1992)

$$\Delta t = a\Delta t_g \tag{5a}$$

and

$$\Delta f = \Delta f_g / a \tag{5b}$$

and indicate that resolutions of the wavelet are simply scaled versions of the time (Δt_g) and frequency (Δf_g) resolutions of the parent wavelet $g(t)$. Physically, the measures provided in Equation (5) indicate that two pulses in time cannot be identified unless they are more than Δt apart. Similarly, two distinct frequency contributions cannot be discerned unless they are more than Δf apart.

While the relationships in Equation (5) seem straightforward, for the Morlet wavelet the issue of resolution is complicated by the fact that it is a Gaussian-windowed Fourier transform. Unfortunately, this window lacks measurable duration. However, by applying Gabor's (1946) definition for mean square measures, an "effective duration" in the time domain and bandwidth in the frequency domain may be identified as (Chui, 1992)

$$\Delta t_g = \frac{1}{\sqrt{2}} \tag{6a}$$

and

$$\Delta f_g = \frac{1}{2\pi\sqrt{2}} \tag{6b}$$

By this definition, the undilated Morlet function evaluated at time t and frequency f effectively windows a portion of the signal from $t - \Delta t_g$ to $t + \Delta t_g$ in the time domain, resulting in a frequency window spanning from $f - \Delta f_g$ to $f + \Delta f_g$. The total area analyzed in the time-frequency domain forms the Heisenberg box, centered at time t and frequency f, shown in Figure 2. Note that the Gaussian window employed by the Morlet wavelet is optimal, that is, it has the same resolution in both the time and angular frequency (ω) domains ($\Delta\omega_g = 2\pi\Delta f_g$).

2.1 Frequency resolution: Modal separation

Having established the resolutions of the Morlet wavelet, the resolutions at a given frequency f_i in the continuous wavelet analysis can be determined by combining Equations (4), (5b), and (6b) to yield

$$\Delta f_i = \frac{f_i}{2\pi\sqrt{2}\, f_o} \tag{7}$$

This dictates that the frequency resolution will improve for longer period signals, an attractive feature of the

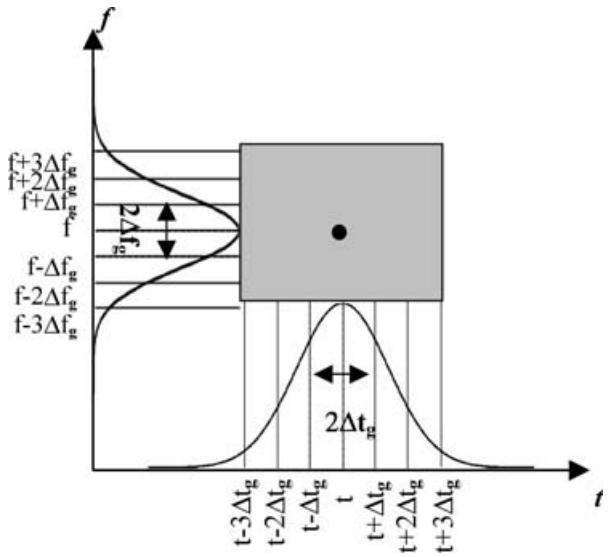

Fig. 2. Effective time and frequency resolutions of undilated Morlet wavelet and associated Heisenburg box.

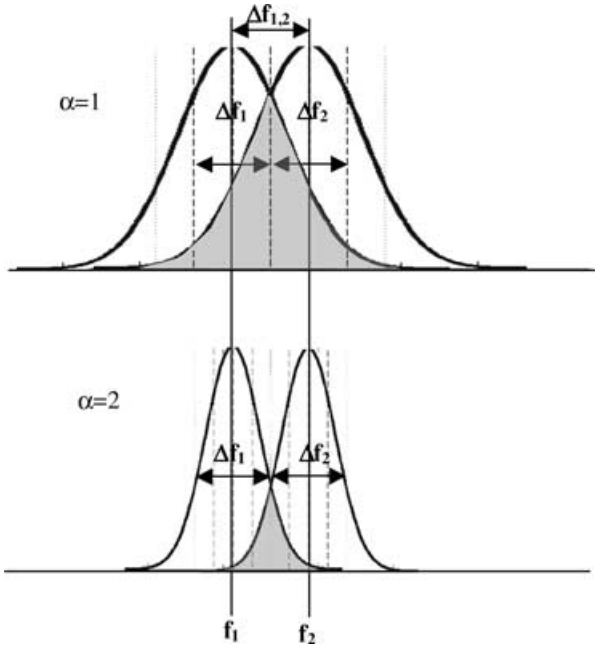

Fig. 3. Schematic demonstration of the implication of parameter selection for modal separation.

wavelet transform, and also implies that the resolution capabilities can be appropriately adjusted for the analysis through careful selection of the central frequency, f_o, of the Morlet wavelet. The effective bandwidth measure for Equation (7) is $2\Delta f_i$. Note, however, that by basing the bandwidth measure on Gabor's mean square estimate for the Gaussian window (see Equation (6b)), only about 68% of the frequency window is accounted for. This measure essentially defines one standard deviation (σ) of the window mean, yielding a frequency window with a total bandwidth $2\Delta_f$ or 2σ, as shown in Figure 2. However, the duration of this frequency window is misleadingly narrow, assuming a better frequency resolution than is truly present. To more strictly define the bandwidth, one should note that roughly 95% of the window lies within two standard deviations of the mean, as also noted in Figure 2, for which the effective bandwidth is $4\Delta_f$ or 4σ. An even stricter condition would extend the definition to three standard deviations, also shown in Figure 2, encompassing 99% of the window. These considerations become important when confronted with the need to separate closely spaced modes.

Therefore, Equation (7) may be generalized, given the need to separate two closely spaced frequency components f_1 and f_2, where the minimum central frequency for an analysis can be determined by

$$f_o = (2\alpha)\frac{f_{1,2}}{2\pi\sqrt{2}\Delta f_{1,2}} \tag{8}$$

$f_{1,2}$ can be taken as either f_1 or f_2 or an average of the two, as the choice has little impact for small values of $\Delta f_{1,2}$, the separation between the two frequency components. α is the parameter defining how much overlap between the adjacent Gaussian windows of the Morlet wavelet is permitted. As shown in Figure 3, using the traditional mean square definition for the bandwidth of the Gaussian window amounts to $\alpha = 1$. As determined by Equation (8), the wavelet analysis windows centered at the two frequencies will overlap significantly. However, increasing α to 2 and applying Equation (8), a larger central frequency is adopted, yielding analysis windows that are narrower, and although centered at the same two frequencies, now have reduced overlap. Note that α can be increased to 3, insuring complete modal separation. As will be shown in a subsequent example, retaining $\alpha = 2$ is typically sufficient to insure adequate modal separation for system identification in most linear systems, although total modal separation via $\alpha = 3$ may be necessary for closely spaced modes when nonlinear system identification is performed.

2.2 Time resolution: End effects

On the other hand, the temporal resolutions of a wavelet analysis have direct bearing on the significance of end effects, which have been noted in a number of applications, for example, Staszewski (1998). In many cases, the *a priori* knowledge of the signal characteristics allows anomalies to be qualitatively distinguished and neglected in subsequent analyses. However, this is, in

general, not possible, requiring a quantitative guideline to establish what portions of the wavelet-transformed signal are accurate. By examining the convolution operation in Equation (1) and the window function in Equation (2), it is evident that, although the wavelet is focused at a given time and represents the temporal content in this vicinity, the window extends into both the past and future (see Figure 2), by an extent dependent on the scale being analyzed. This fact has important implications in the end regions of the wavelet transform map, resulting from the fact that the wavelet analyzed at time t_j spreads half of its analysis window into the past. As Figure 2 illustrates, the undilated analysis window, by the standard RMS definition, spans $2\Delta t_g$. Thus, the temporal duration of the dilated window Δt_i, for the frequency (scale) f_i, is found by combining Equations (4), (5a), and (6a) to yield

$$\Delta t_i = \frac{f_o}{f_i\sqrt{2}} \tag{9}$$

As illustrated in Figure 4, the temporal window is elongated at the lower frequency, f_1. As the analysis time t_j lies within Δt_1 of the ends of the signal, the analysis window extends into a region with no available data, yielding wavelet coefficients based on an "incomplete" signal. Once again, this definition is based on the classical mean square definition in Equation (6a), approximating the effective temporal duration as a single standard deviation of the Gaussian window. Revisiting Figure 2, in light of the previous discussion with respect to frequency resolution, a more stringent condition may be obtained by defining the effective temporal resolution of the Morlet wavelet as 2σ or $2\Delta t_i$, so as to account for about 95% of the Gaussian window. Defining a $3\Delta t_i$ as the temporal resolution can impose an even more stringent condition. Dependent on the desired level of accuracy, either of these conditions can be imposed to quantify the regions potentially at risk to end effects. The general expression

$$\beta\Delta t_i \le t_j \le T - \beta\Delta t_i \tag{10}$$

where β can be set to any nonzero integer value, provides a practical limit on the translations t that can be considered in a wavelet analysis of a signal of length T. Thus, only wavelet coefficients satisfying Equation (10) can be reliably analyzed. Equation (9) dictates that meaningful analyses at low frequencies require larger amounts of data, so that several cycles of the low-frequency phenomena can be retained.

The end effects can have substantial influence on the quality of wavelet coefficients, as discussed in more detail in Kijewski and Kareem (2002b). An illustration of the implications of end effects on instantaneous spectral amplitude is provided in Figure 5, where the calculated instantaneous spectra at each time are plotted one atop the other, essentially collapsing the scalogram in time. In comparison with the theoretical prediction, the improvement in instantaneous spectral amplitude and shape is obvious as the result of progressively neglecting more of the end-effect region, requiring a value of $\beta = 4$ in Equation (10) to sufficiently negate the end-effect phenomenon. However, in the case of more sensitive spectral measures such as the bandwidth, $\beta = 6$ is necessary to eliminate any significant deviation between the theoretical prediction and the wavelet result (Kijewski and Kareem, 2002b,c). Though such deviations are easily explained by the end-effect phenomenon, simply neglecting these regions in analysis results in a considerable loss of data.

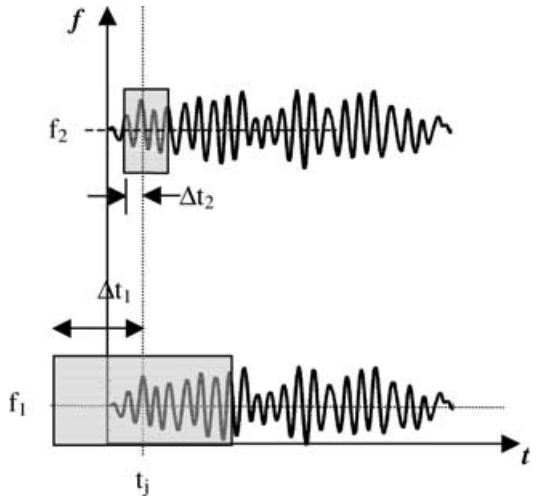

Fig. 4. Illustration of region susceptible to end effects.

2.3 End effects melioration: Signal padding

The loss of considerable regions of a signal is the unfortunate consequence of end effects. One possible solution to this problem would be to pad the beginning and end of the signal with surrogate values, placing the true signal of interest at the center of an elongated vector, and leaving the virtual values at the tails to be corrupted by end effects. In the padding operation detailed in Kijewski and Kareem (2002b), the signal's characteristics are locally preserved by reflecting a portion of the signal about its beginning and end. As the lowest frequency being considered in the analysis f_1 will yield the largest temporal resolution Δt_1, it dictates the maximum end effects anticipated. β is then selected based on the desired accuracy level, and the time ordinates of the sampled time vector

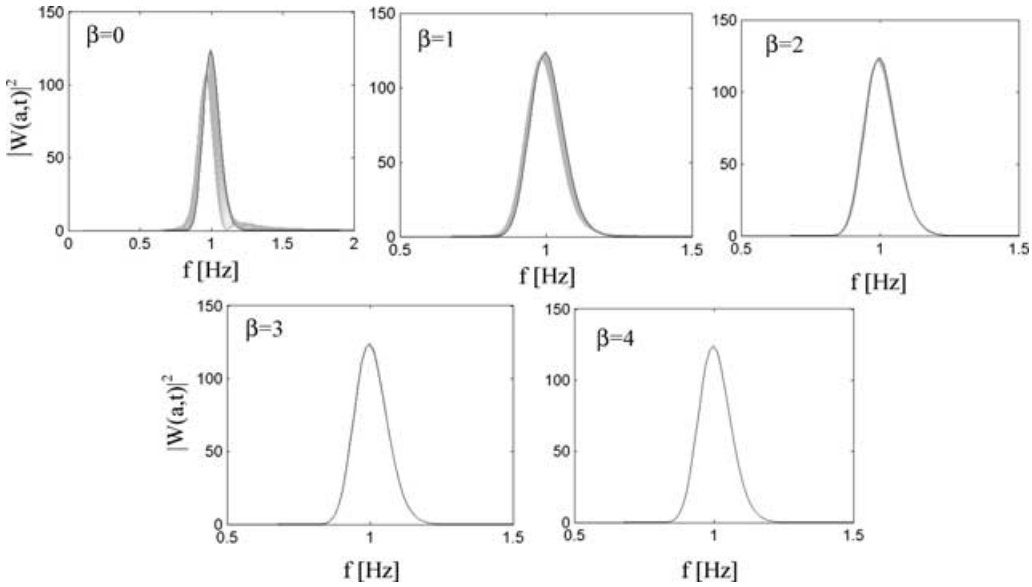

Fig. 5. Deviations of simulated instantaneous spectra (gray) from theoretical result (black) as end-effect regions are progressively neglected.

$t = [t_1 \ \cdots \ t_N]$ closest to the termination of the end-effect regions are then identified by

$$t_n = \min[t > \beta \Delta t_1] \text{ and } t_m = \max[t < (t_N - \beta \Delta t_1)] \tag{11}$$

The modified signal x_{MOD} is constructed by reflecting the signal x (for even functions) or its negative (for odd functions) for the duration of $\beta \Delta t_1$ about t_1 and t_N, according to

$$x_{\text{MOD}} = [\pm x_n \ \pm x_{n-1} \ \cdots \ x_1 \ \cdots \ x_N \ \pm x_{N-1} \ \cdots \ \pm x_m] \tag{12}$$

where x_n and x_m are the values of the sampled signal x at time t_n and t_m. x_{MOD} is then wavelet transformed and the coefficients calculated from the padded regions are simply neglected, retaining only the coefficients of the true signal for meaningful analysis. As discussed in Kijewski and Kareem (2002c), the addition of the padding operation with $\beta = 4$ markedly improves the amplitude of the wavelet coefficients, as well as the bandwidth of wavelet instantaneous spectra, although within $3\Delta t_1$ of the ends the bandwidth still deviates, a result that cannot be fully improved with larger values of β. This is due to the fact that the remaining slight inaccuracies in the amplitude lead to a more marked inaccuracy in the bandwidth measure, being more sensitive. Further illustrations of the merits of this padding operation are discussed in Kijewski and Kareem (2002b,c), whereas subsequent examples in this study will demonstrate the improvements in wavelet-based system identification as a result of this padding operation, as well as the lingering limitations.

3 WAVELET-BASED SYSTEM IDENTIFICATION FOR FREE VIBRATION RESPONSE

Having defined a number of processing considerations relevant to wavelet transforms, this section will introduce the most common means of wavelet-based system identification utilizing Morlet wavelets, which will then be used in subsequent examples to demonstrate the relevance of these processing considerations for civil engineering applications.

The analysis of free vibration or impulse response functions (IRF) from a structure serves as one of the simplest means to identify the frequency and damping in the time domain. In the case of single-degree-of-freedom (SDOF) structures, this identification may be easily conducted using techniques such as the logarithmic decrement, the Hilbert transform, or a least squares fit of the decay curve. However, in cases where multiple degrees of freedom (MDOF) are participating, the identification becomes more involved and necessitates the use of bandpass filtering or more advanced MDOF identification schemes. Recognizing the ability of wavelet transforms to decouple multicomponent signals, a number of researchers began applying this technique in various forms for analysis of impulse (Huang et al., 1994; Robertson et al., 1998a,b) and free vibration response (Hans et al., 2000; Lamarque et al., 2000;

Ruzzene et al., 1997; Staszewski, 1997). The three latter studies drew upon the unique characteristics of Morlet wavelets and the relationships developed for the classical analytic signal and the Hilbert transform, creating a wavelet-based analog capable of accommodating multicomponent signals. It should be noted that the direct application of Hilbert transforms for system identification of MDOF systems was not previously possible, as it explicitly requires a monocomponent signal, necessitating pre-processing through the use of bandpass filtering or techniques such as Empirical Mode Decomposition (Huang et al., 1998; Yang et al., 2000).

The foundations for wavelet-based system identification from IRFs and free vibration response are grounded in the development of the complex analytical signal (Gabor, 1946), taking the form of an exponential function given by

$$z(t) = A(t)e^{i\phi(t)} \tag{13}$$

with time-varying amplitude $A(t)$ and phase $\phi(t)$. From this definition, Ville (1948) proposed the concept of instantaneous frequency as the time-varying derivative of the phase

$$f(t) = \frac{1}{2\pi}\frac{d}{dt}\phi(t) = \frac{1}{2\pi}\frac{d}{dt}\left[\angle z(t)\right] \tag{14}$$

Thus the phase of the complex-valued analytic function provides a simple means to identify the time-varying frequency of the system. In the case of free vibration decay curves, the oscillator responds at the damped natural frequency ω_D, and the time-varying amplitude term takes the form of an exponential, decaying based on the system's natural frequency $\omega_n = 2\pi f_n$ and damping ξ ($\omega_D \sim \omega_n$, for lightly damped systems)

$$z(t) = \left(A_o e^{-\xi\omega_n t}\right) e^{i(\omega_D t+\theta)} \tag{15}$$

where A_o is an initial amplitude value and θ is a phase shift. Note that this complex analytic signal would typically be generated by

$$z(t) = x(t) + i\,H[x(t)] \tag{16}$$

where $x(t)$ is the original signal and the operator $H[\cdot]$ represents the Hilbert transform. Ruzzene et al. (1997) pointed out undesirable behaviors manifested by the use of the Hilbert transform in Equation (16) based on violation of strict asymptotic signal assumptions. Further, the necessary bandpassing operations required for multicomponent signals can be problematic; however, they are simply overcome by employing a transform that directly yields a complex-valued signal, such as the wavelet transform.

As discussed previously, when the Fourier transform of the parent wavelet is sharply concentrated at a fixed value of frequency, as in the case of the Morlet wavelet, the continuous wavelet transform will have the tendency to "concentrate" at the frequency values associated with dominant harmonics in the signal. These locations where the frequency of the scaled wavelet coincides with the local frequency of the signal, denoted by

$$a_r(t) = \frac{\omega_o}{\phi'(t)} = \frac{2\pi f_o}{f_i(t)} \tag{17}$$

are characterized by a high level of similitude resulting in large wavelet coefficients (Mallat, 1998). Note that Equation (17) illustrates that the scales corresponding to the ridges a_r can be directly used to identify the instantaneous frequency, as shown in Figure 1, and further that these ridges are points of stationary phase (Mallat, 1998). By seeking out the points where wavelet coefficients take on local maximum values, according to

$$|W(a_r, t)| = \max_a |W(a, t)| \tag{18}$$

as done in this study, or by seeking out stationarity in the phase, the ridges can be identified (Carmona et al., 1998).

What is important to note is that, in the case of the Morlet wavelet, the real and complex components of the wavelet transform along the ridge are directly proportional to the signal content at that frequency and its corresponding Hilbert transform (Figure 1), yielding a means to directly reproduce Gabor's analytic signal in Equation (13) (Staszewski, 1997). The resulting phase can then be used in Equation (14) to identify the instantaneous frequency, and the amplitude can be fitted according to Equation (15) to determine the damping of the system, as detailed in Ruzzene et al. (1997) and Staszewski (1997, 1998). As this identification can be time varying, piecewise linear fits to the phase and the natural log of the amplitude can be used to identify the system as it evolves with time.

Variations of these concepts, first presented in Ruzzene et al. (1997) and Staszewski (1997), illustrate its applicability to linear system identification. Staszewski (1998) later demonstrated the applicability of the approach for nonlinear systems, where the time-varying estimates of frequency and damping are truly required. Though Staszewski's work (1997, 1998) was primarily directed toward mechanical systems with higher fundamental frequencies, Ruzzene et al. (1997) and Hans et al. (2000) provided examples geared specifically toward civil engineering, applying the techniques to full-scale data. However, as one begins to consider civil engineering structures of longer period, for which the characteristics of narrowbanded response become increasingly prevalent, previously unaddressed processing concerns

highlighted in this study begin to surface and shall be explored through the following examples.

4 SYSTEM IDENTIFICATION FOR FREE VIBRATION: MDOF EXAMPLE

The Morlet wavelet-based analysis allows flexibility in the value of the central frequency f_o to obtain desired resolutions, as discussed previously. This selection becomes critical if closely spaced modes are suspected. Staszewski (1997) discussed the use of shifted Morlet wavelets for separation of closely spaced, high frequency modes; however, in the case of low-frequency systems, the judicious selection of the central frequency of the Morlet wavelet can similarly accomplish the same operation directly. This is illustrated by the analysis of 100 seconds of IRF data (shown in Figure 6), sampled at 10 Hz, for a three-degree-of-freedom system. The stiffness and mass matrices, provided in the Appendix, were selected to achieve a response with both low frequency content and closely spaced modes. The resulting frequencies are 0.567, 1.006 and 1.095 Hz, and all three modes have a critical damping ratio of 0.01. The latter two modes are within 10% of one another, requiring a refined frequency resolution, and thus providing an ideal venue in which to explore the significance of f_o for optimal modal separation.

Without *a priori* knowledge of the system, the selection of a central frequency for analysis should initiate from information gathered through a visual inspection of the time series, as discussed in Kijewski and Kareem (2002a). Such inspection indicates that one obvious period of oscillation is on the order of 1 second. As a general rule of thumb, a frequency resolution of one-tenth the period of oscillation is desirable, that is, $\Delta f_{1,2} = 0.1$ Hz. This serves as a starting point for the analysis and may be refined even further in subsequent analyses to uncover additional details. For the purposes of demonstration, varying levels of α in Equation (8) are used to demonstrate the influence of analysis window overlap in the adjacent frequency bands. Assuming $\alpha = 1$ defaults to a direct application of Gabor's mean square duration and necessitates a minimum wavelet central frequency of 2.25 Hz. To simplify, 3 Hz is chosen for analysis. As suggested previously, $\alpha = 2$ and 3 provide a more accurate means of modal separation. To demonstrate these cases, $f_o = 6$ Hz and 8 Hz wavelet analyses are also performed on the same signal. Table 1 lists the resulting frequency and temporal resolutions as defined by Equations (5) and (6).

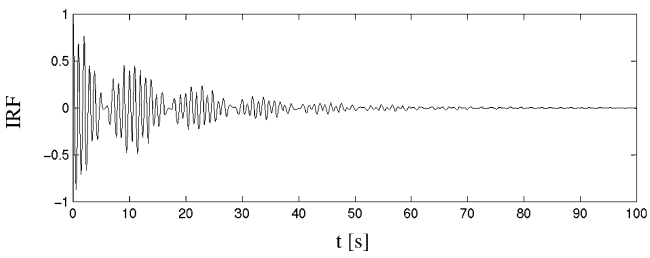

Fig. 6. Impulse response function of MDOF system with closely spaced modes.

4.1 Ridge extraction and wavelet instantaneous spectra

As shown in Figure 7a, the wavelet instantaneous frequencies identified from the ridges for $f_o = 3$ Hz successfully identify the first mode, but have difficulty fully separating the second and third modes, clearly indicating that the choice of central frequency did not provide adequate frequency resolution. The ridge identification becomes very poor beyond 80 seconds—a direct consequence of the diminished amount of signal energy at this point and demonstration of the influence of end effects. Figure 7b reveals that separation was possible for $f_o = 6$ Hz, again with some difficulty at the final seconds of the signal. The analysis for $f_o = 8$ Hz in Figure 7c merely extends the end-effect region deeper into the signal. With the introduction of the aforementioned padding scheme to $f_o = 6$ Hz, the slight end effects at the initiation of the signal are remedied in Figure 7d and diminished at the termination of the signal, although the lack of signal energy in this region makes identification of the highest mode difficult. In general, the influence of end effects is not observed to significantly influence ridge frequencies (Kijewski and Kareem, 2002c). Instantaneous spectra are provided in Figure 8, demonstrating the concentration of energy at the ridge frequencies. Note that Figures 8a and b demonstrate the intermittency of modal separation evident in the first mode ridge (Figure 7a) for the $f_o = 3$ Hz analysis. Further, the progressive narrowing of the instantaneous spectral bandwidth within the frames, thereby indicating more complete modal separation, illustrates the refinement of frequency resolution as central frequency is increased.

4.2 Wavelet skeletons and end effects

The wavelet skeleton can be extracted from the ridges identified in Figure 7, with the real component being proportional to the signal itself. Figure 9a reiterates the inability of the $f_o = 3$ Hz analysis to separate the two higher modes. The analyses in Figures 9b and c demonstrate that such modal separation is possible with sufficient frequency resolution. It was noted in Kijewski and Kareem (2002c) that, in general, the wavelet

Table 1
Wavelet-based identification of MDOF system with closely spaced modes

	Resolutions		*Actual*		*Analytic signal ID*			*Ridge IF & Log Dec ID*		
Mode	$\Delta t_i(s)$	$\Delta f_i(Hz)$	$avg[f_n]$ *(Hz)*	$avg[f_n]$ *(Hz)*	$avg[f_n]$ *(Hz)*	$avg[\xi]$	$CoV[\xi]$	$avg[f_n]$ *(Hz)*	$avg[\xi]$	$CoV[\xi]$
				$f_o = 3$ Hz, $\beta = 0$						
1	3.74	0.021	0.567	0.01	Incomplete modal separation					
2	2.11	0.038	1.006	0.01						
3	1.94	0.041	1.095	0.01						
				$f_o = 6$ Hz, $\beta = 0$						
1	7.49	0.011	0.567	0.01	0.567	0.0098	4.48%	0.566	0.0099	4.61%
2	4.21	0.019	1.006	0.01	1.006	0.0099	4.43%	1.005	0.0099	8.15%
3	3.87	0.020	1.095	0.01	1.095	0.0098	10.0%	1.094	0.0098	10.4%
				$f_o = 8$ Hz, $\beta = 0$						
1	9.98	0.008	0.567	0.01	0.567	0.0098	6.58%	0.565	0.0097	5.93%
2	5.62	0.014	1.006	0.01	1.006	0.0098	4.79%	1.008	0.0097	9.48%
3	5.17	0.015	1.095	0.01	1.095	0.0098	3.98%	1.098	0.0096	12.5%
				$f_o = 6$ Hz, $\beta = 4$						
1	7.49	0.011	0.567	0.01	0.567	0.0099	1.12%	0.566	0.0100	2.47%
2	4.21	0.019	1.006	0.01	1.006	0.0100	1.53%	1.005	0.0101	7.09%
3	3.87	0.020	1.095	0.01	1.095	0.0100	8.93%	1.095	0.0100	13%
				$f_o = 8$ Hz, $\beta = 4$						
1	9.98	0.008	0.567	0.01	0.567	0.0099	1.74%	0.565	0.0099	2.91%
2	5.62	0.014	1.006	0.01	1.006	0.0100	1.13%	1.008	0.0101	8.58%
3	5.17	0.015	1.095	0.01	1.095	0.0100	0.91%	1.098	0.0098	10.4%

skeletons are not capable of accurately capturing the amplitude of the signal for the first $3\Delta t_i$ due to the end-effect phenomenon, requiring $\beta = 3$ in Equation (10). These critical regions are marked by the vertical dotted line in each plot. Within this region, the initiation of the impulse response function manifests a rounded hump, very evident from the second mode in Figures 9b and c. In addition, at the end of the signal, a flare in amplitude also occurs in this $3\Delta t_i$ region, intensifying with time. Particularly in the case of $f_o = 8$ Hz, the end-effect regions for the first mode can consume a significant portion of the signal. It becomes evident that for high-resolution analyses, the end effects at low frequencies leave little useable signal for reliable system identification. Note that such marked end effects were not apparent in previous work due to the smaller central frequencies employed, as a result of the attention toward higher frequency phenomenon and the lack of closely spaced modes. However, in the analysis of many civil engineering structures, such manifestations should be expected. In an effort to diminish the presence of end effects, the aforementioned padding procedure is employed in Figure 9d, revealing

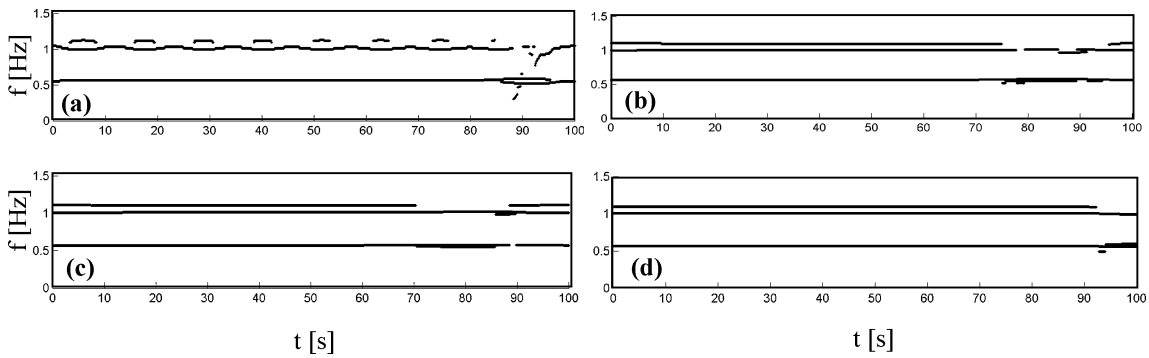

Fig. 7. Instantaneous frequencies identified from ridges of wavelet transform for (a) $f_o = 3$ Hz, (b) $f_o = 6$ Hz, (c) $f_o = 8$ Hz, and (d) $f_o = 6$ Hz with padding.

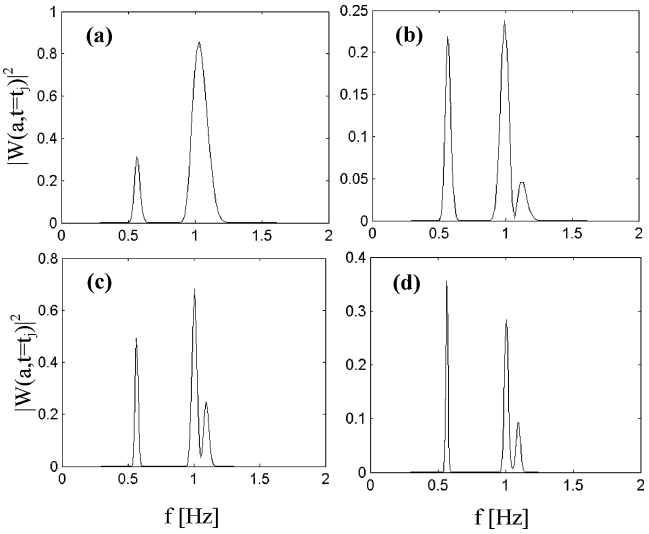

Fig. 8. Instantaneous wavelet spectra for (a) $f_o = 3$ Hz when two modes are present, (b) $f_o = 3$ Hz when three modes are present, (c) $f_o = 6$ Hz, and (d) $f_o = 8$ Hz.

the marked improvement in the wavelet approximations of the signal (Kijewski and Kareem, 2002b,c), shifting the vertical bars denoting the $3\Delta t_i$ regions engulfed by end effects to $t = 0$ and $t = T = 100$ seconds.

4.3 System identification via wavelet amplitude and phase

Figure 10 displays the phase and amplitude curves of the wavelet-transformed data for each mode, later used to identify frequency and damping for the $f_o = 6$ and 8 Hz analyses, which produced meaningful wavelet skeletons. For this system with constant dynamic properties, these should be straight lines, although some minor rippling occurs in the amplitude envelopes, particularly near the end-effects region. Using the analytic signal theory discussed previously, the frequency and damping may be identified via Equations (14) and (15) through a piecewise linear fit to the phase and the natural log of the wavelet amplitude along the ridges, respectively. While the identification of frequency is generally not difficult, damping proves to be a far more elusive parameter to identify. As shown in Figure 11, the piecewise fits of the amplitude curves in Figure 10 produce damping estimates that gradually approach the actual damping of 0.01. The initial inaccuracies are the result of end effects, producing negative values of damping in Figures 11a and c due to the rounding of the skeleton shown in Figures 9b and c. As outlined in Kijewski and Kareem (2002c), without padding, damping values do not stabilize until $5\Delta t_i$, marked by the third vertical bar in each plot. By

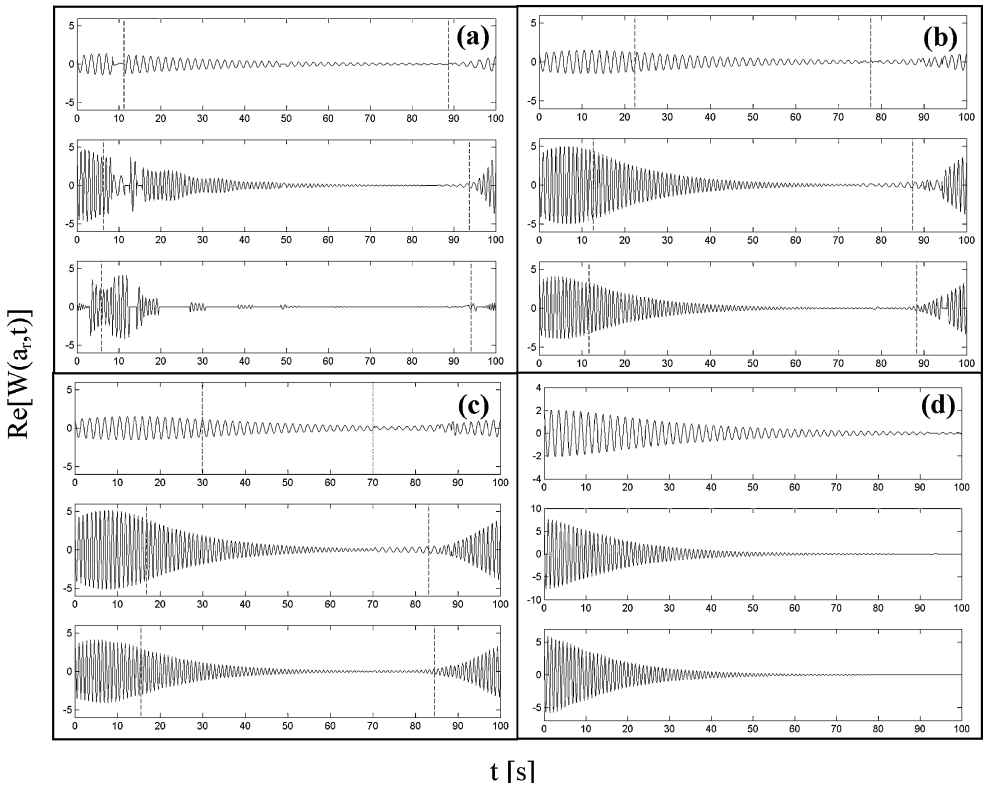

Fig. 9. Real component of wavelet skeleton: each panel contains skeleton for the ridge associated with modes 1, 2, and 3, respectively, for (a) $f_o = 3$ Hz, (b) $f_o = 6$ Hz, (c) $f_o = 8$ Hz, and (d) $f_o = 6$ Hz with padding. Dotted vertical line demarks the $3\Delta t_i$ region of end effects.

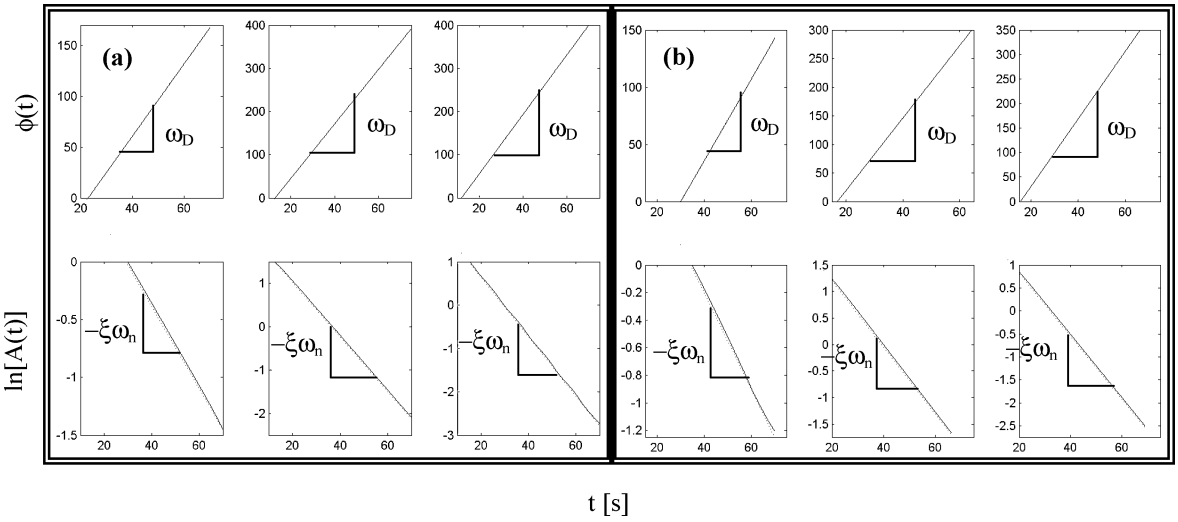

Fig. 10. Wavelet phase and amplitude curves for system identification of MDOF system (solid line) with linear least squares fit (dotted line), for (a) $f_o = 6$ Hz and (b) $f_o = 8$ Hz. Each panel contains data for modes 1, 2, and 3 from left to right.

introducing the padding operation, Figures 11b and d, do not manifest negative damping and stabilize within $3\Delta t_i$. As discussed in Kijewski and Kareem (2002b), the manifestation of end effects in the wavelet amplitudes can be minimized through the simple padding procedure presented here; however, slight inaccuracies in the amplitude remain, of the order of a few percent, for the first $3\Delta t_i$. For the more sensitive bandwidth measures, the presence of even slight errors in the amplitude translates into more significant deviations in parameters such as damping. Still, the introduction of padding eliminates negative damping estimates and stabilizes the damping estimate sooner, although system identification for the purpose of damping estimation should not be performed on the first or last $3\Delta t_i$ of the wavelet skeleton. In light of this, the fact that many civil engineering structures possess very low levels of damping is actually a benefit, as the IRFs will take longer to decay, leaving adequate amounts of data for analysis despite neglecting some regions.

By constraining the identification of the system to the regions beyond $3\Delta t_i$ of ends, the frequency and damping can be identified on average with considerable accuracy, as summarized in Table 1. The natural frequencies of the system show little fluctuation and are identified with precision and manifest little sensitivity to end effects. The

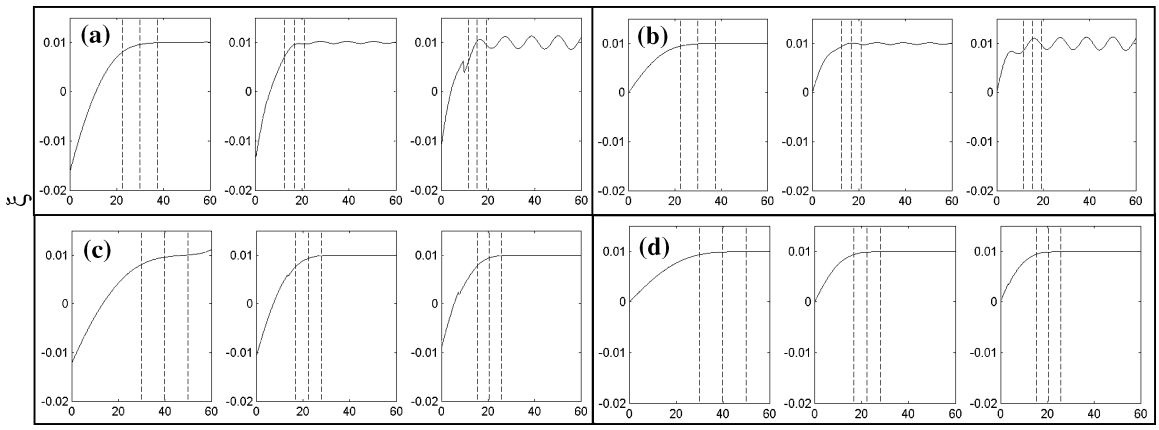

Fig. 11. Identification of damping from piecewise fit to amplitude curves of MDOF system for (a) $f_o = 6$ Hz, (b) $f_o = 6$ Hz with padding, (c) $f_o = 8$ Hz, and (d) $f_o = 8$ Hz with padding. Each panel contains data for modes 1, 2, and 3 from left to right. Dotted vertical line demarks the $3\Delta t_i$, $4\Delta t_i$, and $5\Delta t_i$ end-effect regions.

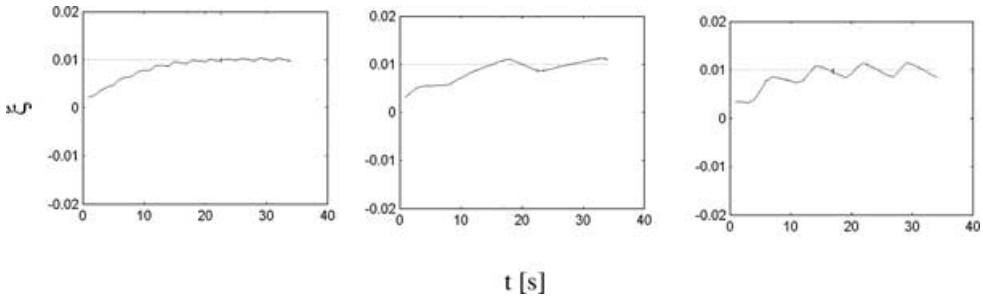

Fig. 12. Identification of damping via logarithmic decrement of wavelet skeleton for $f_o = 8$ Hz with padding. Modes 1, 2, and 3 shown from left to right.

damping estimates, in terms of their mean and coefficient of variation (CoV), are also quite reliable, although they temporally vary. The introduction of padding to the systems, results in a decrease in the CoV, again affirming the efficacy of this pre-processing tool. The increase in central frequency does not markedly affect the statistics of the damping estimation, although Figure 11 demonstrates that the behavior temporally is more reasonable. Therefore, if estimates of frequency and damping are to be obtained for a known linear system, a linear fit to the entire curve in Figure 10 may be performed to yield estimates similar to the averaged quantities in Table 1, and a value of $\alpha = 2$ should be sufficient. However, in the case of nonlinear systems, as explored by Staszewski (1998), a piecewise analysis is necessary to capture time-varying dynamic properties. However, note the rippling of damping estimates in the $f_o = 6$ Hz analysis (Figures 11a and b). The rippling in this case is indicative of incomplete modal separation. While the frequency ridges in Figure 7b indicated that separation was successful, it is again the more sensitive damping measure that verifies that the bandwidths of the two systems are still slightly overlapping. This is evident when comparing Figures 8c and d. The increase in f_o eliminates this spurious behavior (Figures 11c and d), although again at the expense of temporal resolution, requiring some compromise between achieving modal separation and minimizing end effects. Unfortunately, a choice of too small a f_o may produce rippling such as that in Figure 11a that may be mistaken for nonlinear behavior. Therefore, if the assumption of a linear system cannot be safely made, $\alpha = 3$ may be more appropriate for time-varying system identification.

For comparison, the frequencies corresponding to the scales (frequencies) of the ridges are listed in Table 1 and are reasonably accurate estimates of the natural frequency. As a result, for time-frequency analysis such as that presented in Kijewski and Kareem (2002a), frequencies can usually be identified solely from the amplitude of the wavelet transform for $\alpha = 1$ or $\alpha = 2$ if closely spaced modal components are suspected. For further comparison, an alternative means for damping estimation is provided by a logarithmic decrement approach applied to wavelet skeletons (Hans et al., 2000; Lamarque et al., 2000). Such an approach, being reliant on the peaks of the amplitude decay, is more susceptible to fluctuations, particularly in the higher modes, even when modal separation is achieved. Figure 12 demonstrates this for the logarithmic decrement identification of damping for $f_o = 8$ Hz with padding applied. Note that the stabilization trend in the damping witnessed in Figure 11 is again apparent, although with more irregular variations. The statistics of the logarithmic decrement identification are also provided in Table 1 for comparison and reveal that the damping estimates are reasonable in the mean. Without padding, the CoV of the logarithmic decrement results is comparable to those obtained using the method based on analytic signal theory. However, when padding is applied and complete modal separation is assured ($f_o = 8$ Hz, $\beta = 4$), the CoV of the logarithmic decrement technique is significantly larger than the other identification approach presented, especially for the higher modes. This highlights that much of the variance in damping identified by the analytic signal approach is merely due to end effects and the lack of modal separation.

5 SYSTEM IDENTIFICATION FROM AMBIENT VIBRATION DATA: FULL-SCALE EXAMPLE

Obtaining the IRF or free vibration curve can be difficult if not impossible for many civil engineering structures, so there is interest in developing approaches to permit the extraction of decay curves from ambient vibration data. The random decrement technique (RDT) has evolved as a popular analysis tool that applies the use of a trigger condition to capture segments of ambient time histories possessing the same amplitude and slope (Cole, 1973; Gurley and Kareem, 1996). Subsequent averaging

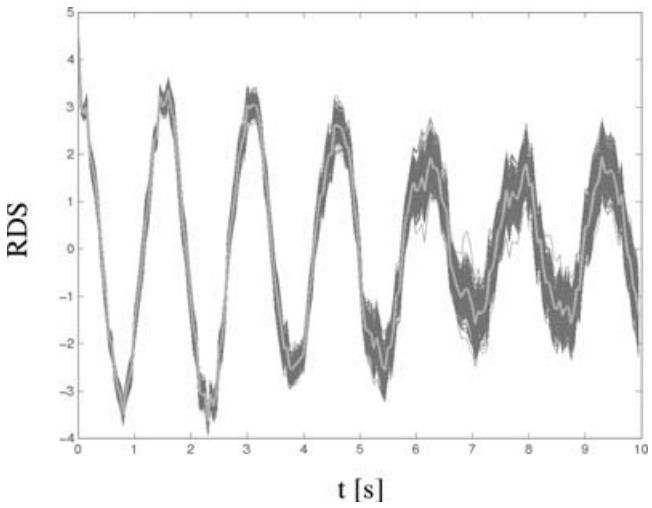

Fig. 13. Example of random decrement signature (gray) and variance envelope.

of these segments yields a random decrement signature (RDS), which is proportional to the free vibration curve of mechanical systems. Though Ruzzene et al. (1997) employed this technique to analyze full-scale bridge data, some added concerns surface when the wavelet system identification approach discussed here is merged with the RDT for low-frequency systems. It has been shown that the variance of RDS signatures increases with each cycle of oscillation (Vandiver et al., 1982) as one moves further from the trigger condition, indicating that system identification should be restricted to the first few cycles of the RDS. Through a bootstrap resampling scheme developed by Kijewski and Kareem (2002d), an envelope of variance in a random decrement signature may be visualized, as presented in Figure 13. The figure illustrates the limited number of cycles over which identification can be reasonably made. The degradation of decrement signatures is problematic for low-frequency civil engineering structures, when wavelets are employed, since the end-effect region described in Equation (10) lengthens. While padding does repair the amplitudes considerably, reliable damping identification should only proceed outside of the $3\Delta t_i$ end-effect region, although frequency identification and signal amplitude reconstruction remains viable throughout. The amount of data lost can be offset to some extent by decreasing the analyzing frequency f_o of the Morlet wavelet, albeit compromising the ability to distinguish closely spaced modes. This permits the identification of damping from more reliable portions of the RDS.

To illustrate, the RDT is applied to 1.5 hours of acceleration data, sampled at 20 Hz and shown in Figure 14. The data were measured along the y-axis of a tower in Japan during a typhoon (Tamura et al., 1993). Note that

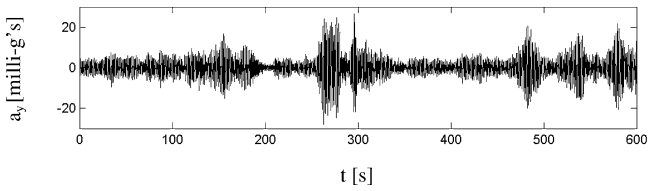

Fig. 14. Ten minutes of acceleration response (y-direction) of tower in typhoon.

during simple free vibration tests, the tower was found to have a fundamental sway period of 1.6 seconds in both directions, with a critical damping ratio of 0.015. The application of RDT, with 225 averaged segments, yields the signature shown in Figure 15a. Note that the signature lacks the smooth characteristic one would anticipate from a decay of a SDOF damped oscillator, indicating the presence of higher modes or other noise in the RDS, which would normally have to be separated through some bandpass filtering. Such modal separation is achieved using a $f_o = 0.5$ Hz Morlet wavelet transform. The low value of central frequency was chosen so as to maximize the amount of usable transformed signal in light of the competing restrictions of variance in the random decrement signature and the end effects of the wavelet transform, minimized to some extent with the padding operation. The real component of the wavelet coefficients, given in Figure 15b, identifies a single mode contributing to the response, as typically observed under wind excitation, and the decaying oscillatory character of the decrement signature. The breadth of the scalogram in the frequency domain reiterates the loss in frequency resolution, which resulted from the choice of a Morlet wavelet with superior time resolution. The skeleton extracted from the ridge of the wavelet is shown in Figure 15c and is clean and smooth, as the wavelet transform has separated the higher frequency noise in the RDS in Figure 15a. The RDS embodied by the skeleton appears to be relatively stable up to about 10 seconds, after which it degrades in quality as a result of the increasing variance shown in Figure 13. As a result, the system identification should be performed at most on the first 10 seconds of the RDS. Figure 15d shows a comparison between the signature in the first 10 seconds and the anticipated signature, based on the structure's known frequency and damping. Inconsistencies in amplitude and phase between the two propagate with time, as a result of RDS variance, and suggest that system identification should be performed within the first 3–4 seconds of the RDS. Though the comparison in Figure 15d is not available during the typical system identification process, the variance envelopes shown in Figure 13 allow the user to make a similar conclusion that the RDS quality is suspect beyond 4 seconds.

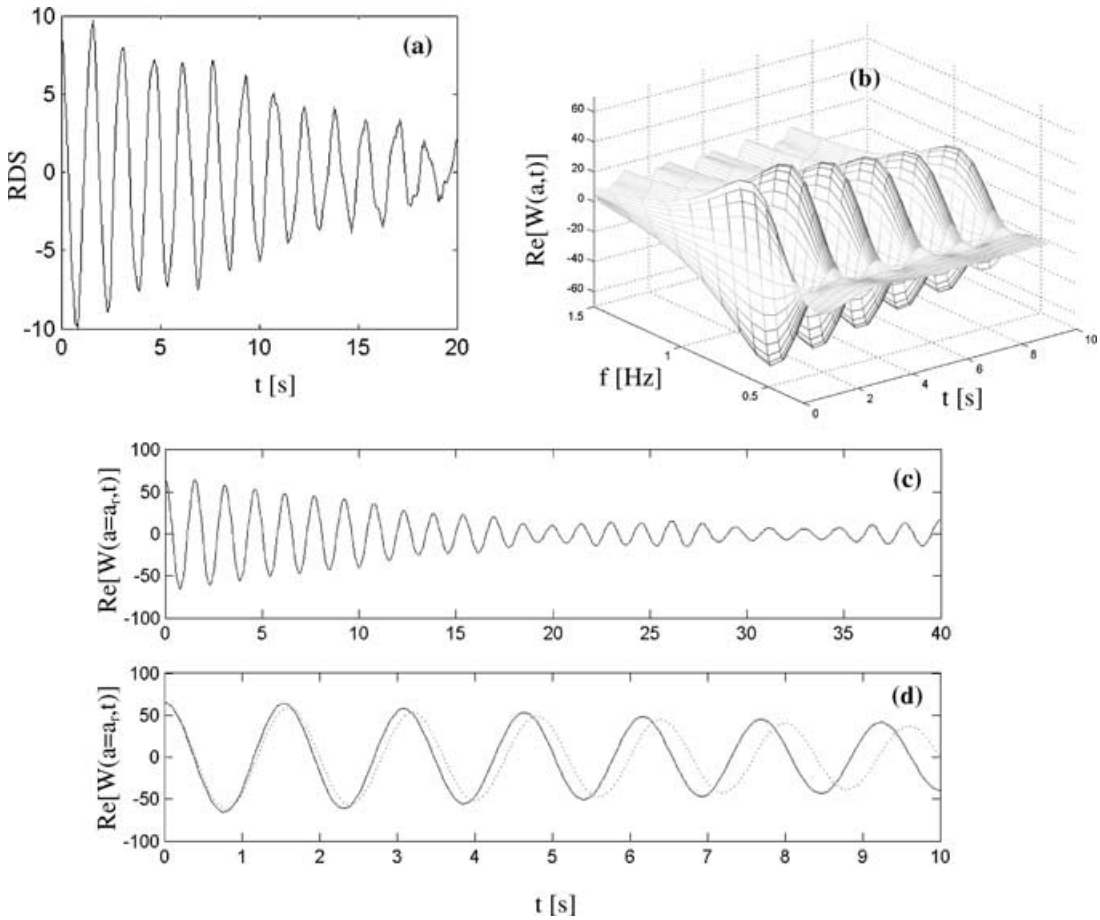

Fig. 15. (a) Random decrement signature, (b) real component of wavelet-transformed random decrement signature in 3D, (c) real-valued skeleton, (d) zoom of real-valued skeleton (solid line) with theoretical skeleton (dotted line) for $f_n = 0.625$ Hz and $\xi = 0.015$.

As discussed previously, due to minor end effects remaining in spite of padding, identification of damping should proceed beyond $3\Delta t_1$ of the initiation of the wavelet-transformed random decrement signature. Thus the useable portion of the RDS may be first defined as, $t_{\text{use}} = 1.657$ to 10 seconds. The end-effect region was minimized as a result of compromising frequency resolution, which will not significantly affect the results for this system since no closely spaced modes are present. Identification of frequency and damping by the procedure based on analytic signal theory produced estimates of frequency and damping shown in Figures 16a and c. Note that beyond 10 seconds, the quality of estimates rapidly degrades, due to the variance of the RDS. Zooming in on the first 10 seconds in Figures 16b and d reaffirms two previous observations: the identified frequency suffers very little as the result of end effects, and even with the padding operation, damping estimates are less reliable in the first $3\Delta t_1$ (marked by the dashed line in Figure 16d) although gradually approaching more stable levels. As summarized in Table 2, piecewise fits of the amplitude and phase of the RDS over only t_{use} produced mean frequency and damping estimates consistent with that observed from free vibration testing, although with considerable variance in the damping estimate. Note that the tracking of nonlinear frequency and damping characteristics via the random decrement technique, discussed by Tamura and Suganuma (1996), can be accomplished by varying the trigger condition on captured segments. The resulting decrement signature will manifest, in its first few reliable cycles, the frequency and damping referenced to the amplitude level defined by the trigger. Therefore, the RDS associated with a given trigger level can be assumed linear and any nonlinearity will be evident as the trigger level is changed and other RDS are analyzed.

In such cases where the RDS is known to represent a linear system, it is more reasonable to conduct a best fit of the entire length of t_{use} to smooth out any variation, as shown in Figures 16e and f. Note that there is still

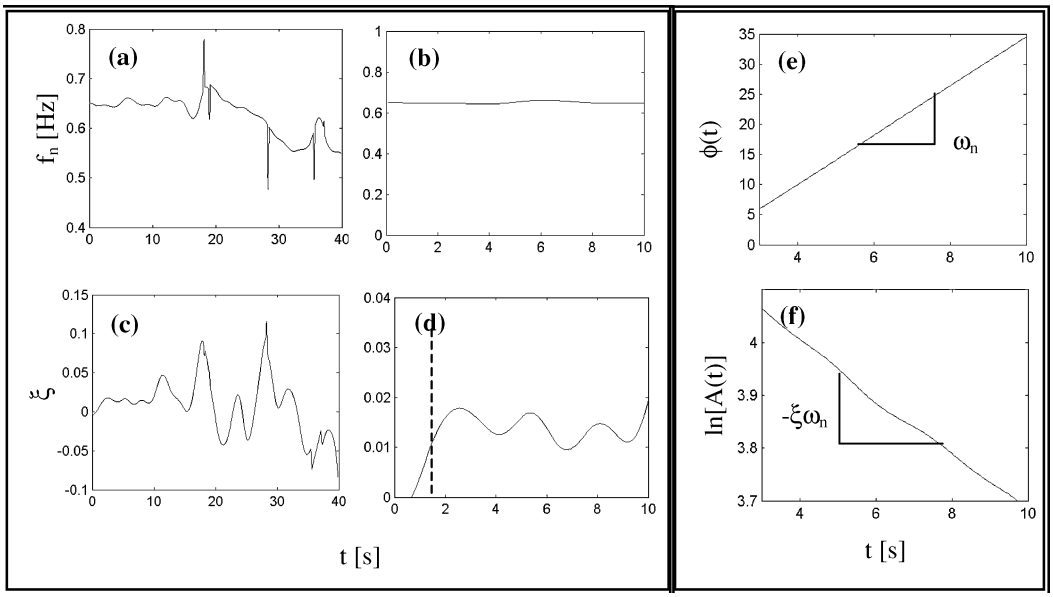

Fig. 16. (a) Frequency and (c) damping identified from wavelet skeleton, zoom of (b) frequency and (d) damping estimates, (e) wavelet phase along ridge, (f) wavelet amplitude along ridge.

Table 2
Wavelet-based identification from full-scale ambiently-excited data

Measured in free vibration test		*Identified piecewise over* t_{use}			*Identified from* $t_{use} = 3\Delta t_1$–*10 s*		*Identified from* $t_{use} = 3\Delta t_1$–*4 s*	
f_n *(Hz)*	ξ	f_n *(Hz)*	*avg*[ξ]	*CoV*[ξ]	f_n *(Hz)*	ξ	f_n *(Hz)*	ξ
0.625	0.0150	0.650	0.0141	18.43%	0.651	0.0136	0.645	0.0151

a slight deviation in the log of the amplitude, producing a slightly smaller damping estimate than the piecewise mean. However, re-inspection of Figure 15d reveals that significant deviations in phase and amplitude in the decrement signature are evident beyond the 4th second, a fact affirmed by Figure 13. Therefore, restricting the identification to $t_{\text{use}} = 1.657$ to 4 seconds, is more reasonable. The resulting estimates of damping (0.0151) and frequency (0.645 Hz) are both within a few percent of the values observed in free vibration test. These results are also consistent with the findings of Tamura et al. (1993) from data collected during the passage of several typhoons. The results in Table 2 and Figure 16 highlight the importance of identification in the early stages of the degrading random decrement signatures. It is interesting to note that Ruzzene et al. (1997) found some discrepancy between the identified damping values and those observed previously by other techniques, possibly due to estimation of damping from the later, less-reliable cycles of the RDS. Such characteristics of the RDT make it vital that the end effects issues in wavelet transformed random decrement signatures are recognized and accounted for to insure reliable system identification.

6 CONCLUSIONS

The wavelet transform, by virtue of its multiresolution, time-frequency analysis capabilities, is gaining popularity, not only for identification of time-varying frequency content, but also for total system identification of multi-degree-of-freedom systems. In particular, the Morlet wavelet has become a popular choice by virtue of its direct relationship to the Fourier transform. However, the application of this parent wavelet for any analysis, including system identification, must be done with care, in light of the ramifications of the resolutions chosen for the analysis. These considerations become significant for civil engineering structures, whose dynamics are often more narrowbanded than traditional mechanical systems. As a result, this study introduced guidelines for modal separation, revealing that the

classical mean square frequency bandwidth definition for Morlet wavelet analysis does not accurately capture the full bandwidth of the analysis. Rationalized in light of the characteristics of Gaussian windows, doubling this bandwidth can separate closely spaced modes permitting reliable identification of averaged frequency and damping in known linear systems. However, if time-varying dynamic properties are to be tracked in nonlinear systems with potentially closely spaced modes, complete modal separation and stability of damping estimates requires tripling the classical mean square bandwidth measure.

In addition, the study explored the end-effect phenomenon, which is more marked for low-frequency civil engineering structures and introduced a padding procedure that repairs the amplitude of wavelet skeletons, eliminates the appearance of negative damping, and more quickly stabilizes the behavior of damping estimates, reducing their coefficient of variation. However, the sensitivity of the damping measure still results in some inaccuracy within $3\Delta t_i$ of the ends, defining the acceptable analysis regimes of the transformed signal.

Examples reiterated these findings and demonstrated that proper selection of Morlet wavelet central frequencies is important to balance modal separation and the length of usable signal for system identification, an important consideration when the random decrement technique is applied for analysis of ambient vibration data. The examples further confirmed that the instantaneous frequency, identified from the wavelet phase or from ridges of the amplitude is relatively insensitive to end effects. A comparison of the wavelet-identification scheme based on analytic signal theory and a wavelet logarithmic decrement revealed the latter's susceptibility to fluctuations, although in a mean sense; both techniques performed equally well for damping identification of linear systems. It was observed that when adequate modal separation was achieved and when padding was applied, the coefficient of variation in the analytic signal approach is quite low, highlighting that much of the variance in damping estimates may be attributed to end effects and modal overlap and not the identification technique itself.

ACKNOWLEDGMENTS

The authors gratefully acknowledge support from NSF Grant CMS 00-85109, the NASA Indiana Space Grant and the Center for Applied Mathematics at the University of Notre Dame. The authors would also like to thank Dr. Yukio Tamura of the Tokyo Institute of Polytechnics for providing the full-scale tower acceleration data.

REFERENCES

Carmona, R. A., Hwang, W. L. & Torresani, B. (1998), *Wavelet Analysis and Applications: Practical Time-Frequency Analysis*, vol. 9, Academic Press, San Diego.

Chui, C. K. (1992), *Wavelet Analysis and Applications: An Introduction to Wavelets*, vol. 1, Academic Press, San Diego.

Coca, D. & Billings, S. A. (1997), Continuous-time system identification for linear and nonlinear systems using wavelet decompositions, *International Journal of Bifurcation and Chaos*, **7**(1), 87–96.

Cole, H. A. (1973), On-line failure detection and damping measurement of aerospace structures by random decrement signatures, *NASA CR-2205*.

Corbin, M., Hera, A. & Hou, Z. (2000), Locating damage regions using wavelet approach, in *Proceedings of 14th ASCE Engineering Mechanics Conference*, Austin, May 21–24, CD-ROM.

Gabor, D. (1946), Theory of communication, *Proceedings of IEEE*, **93**(III), 429–57.

Ghanem, R. & Romeo, F. (2000), A wavelet-based approach for the identification of time-varying dynamical systems, *Journal of Sound and Vibration*, **234**(4), 555–76.

Grossman, A. & Morlet, J. (1990), Decompositions of functions into wavelets of constant shape and related transforms, in L. Streit, (ed.), *Mathematics and Physics, Lecture on Recent Results*, World Scientific, Singapore, 135–65.

Gurley, K. & Kareem, A. (1996), Damping in structures: its evaluation and treatment of uncertainty, *Journal of Wind Engineering and Industrial Aerodynamics*, **59**(2,3), 131–57.

Gurley, K. & Kareem, A. (1999), Applications of wavelet transforms in earthquake, wind and ocean engineering, *Engineering Structures*, **21**, 149–67.

Gurley, K., Kijewski, T. & Kareem, A. (2003), Higher-order correlation detection in nonlinear aerodynamic systems using wavelet transforms, *ASCE Journal of Engineering Mechanics*, **129**(2), 188–201.

Hans, S., Ibraim, E., Pernot, S., Boutin, C. & Lamarque, C.-H. (2000), Damping identification in multi-degree-of-freedom systems via a wavelet-logarithmic decrement—part 2: Study of a civil engineering building, *Journal of Sound and Vibration*, **235**(3), 375–403.

Hartin, J. R. (2001), Application of a wavelet based FRF to the analysis of a bilinear structure, in *Proceedings of International Modal Analysis Conference*, Orlando, February 5–8, 1414–19.

Huang, S. Y., Qi, G. Z. & Yang, J. C. S. (1994), Wavelet for system identification, in *Proceedings of International Modal Analysis Conference*, Honolulu, 1162–66.

Huang, N. E., Shen, Z., Long, S. R., Wu, M. C., Shih, H. H., Zheng, Q., Yen, N.-C., Tung, C. C. & Lu, H. H. (1998), The empirical mode decomposition and the Hilbert spectrum for nonlinear and non-stationary time series analysis, *Proceedings of Royal Society of London*, **454**, 903–95.

Kijewski, T. & Kareem, A. (2002a), Time-frequency analysis: revisiting the efficacy of Hilbert spectra and wavelet transforms, *Proceedings of Royal Society A*, in review.

Kijewski, T. & Kareem, A. (2002b), On the presence of end effects and associated remedies for wavelet-based analysis, *Journal of Sound and Vibration*, **256**(5), 980–88.

Kijewski, T. & Kareem, A. (2002c), Wavelet transforms for system identification and associated processing concerns, in *Proceedings of ASCE Engineering Mechanics Conference*, Columbia University, New York, June 2–6.

Kijewski, T. & Kareem, A. (2002d), On the reliability of a class of system identification techniques: insights from bootstrap theory, *Structural Safety*, **24**(2–4), 261–80.
Lamarque, C.-H., Pernot, S. & Cuer, A. (2000), Damping identification in multi-degree-of-freedom systems via a wavelet-logarithmic decrement—part 1: Theory, *Journal of Sound and Vibration*, **235**(3), 361–74.
Mallat, S. (1998), *A Wavelet Tour of Signal Processing*, Academic Press, San Diego.
Robertson, A. N., Park, K. C. & Alvin, K. F. (1998a), Extraction of impulse response data via wavelet transform for structural system identification, *Transactions of the ASME*, **120**, 252–60.
Robertson, A. N., Park, K. C. & Alvin, K. F. (1998b), Identification of structural dynamics models using wavelet-generated impulse response data, *Transactions of the ASME*, **120**, 261–66.
Ruzzene, M., Fasana, A., Garibalidi, L. & Piombo, B. (1997), Natural frequencies and dampings identification using wavelet transform: application to real data, *Mechanical Systems and Signal Processing*, **11**(2), 207–18.
Staszewski, W. J. (1997), Identification of damping in MDOF systems using time-scale decomposition, *Journal of Sound and Vibration*, **203**(2), 283–305.
Staszewski, W. J. (1998), Identification of non-linear systems using multi-scale ridges and skeletons of the wavelet transform, *Journal of Sound and Vibration*, **214**(4), 639–58.
Staszewski, W. J. & Giacomin, J. (1997), Application of the wavelet-based FRFs to the analysis of nonstationary vehicle data, in *Proceedings of International Modal Analysis Conference*, Orlando, 425–31.
Tamura, Y., Shimada, K. & Kazuki, H. (1993), Wind response of a tower (typhoon observation at the Nagasaki Huis Ten Bosch Domtoren), *Journal of Wind Engineering & Industrial Aerodynamics*, **50**, 309–18.
Tamura, Y. & Suganuma, S.-Y. (1996), Evaluation of amplitude-dependent damping and natural frequency of buildings during strong winds, *Journal of Wind Engineering & Industrial Aerodynamics*, **59**(2,3), 115–30.
Vandiver, J. K., Dunwoody, A. B., Campbell, R. B. & Cook, M. F. (1982), A mathematical basis for the random decrement vibration signature analysis technique, *Journal of Mechanical Design*, **104**, 307–13.
Ville, J. (1948), Theorie et application de la notion de signal analytical, *Cables et Transmissions*, **2A**(1), 61–74.
Yang, J. N., Kagoo, P. K. & Lei, Y. (2000), Parametric identification of tall buildings using ambient wind vibration data, in A. Kareem, A. Haldar, B. F. Spencer & E. A. Johnson, (eds.), *ASCE Specialty Conference on Probabilistic Mechanics and Structural Reliability*, University of Notre Dame, July 24–26, CD-ROM, PMC2000-076.

APPENDIX

The impulse response of a MDOF described by

$$\boldsymbol{m}\ddot{\boldsymbol{x}} + \boldsymbol{c}\dot{\boldsymbol{x}} + \boldsymbol{k}\boldsymbol{x} = \boldsymbol{\delta}(t) \tag{A.1}$$

where $\boldsymbol{m}$, $\boldsymbol{c}$, and $\boldsymbol{k}$ are the mass, damping and stiffness matrices, respectively; $\boldsymbol{x}$ is the vector of displacements; $\dot{\boldsymbol{x}}$ and $\ddot{\boldsymbol{x}}$ are the first and second derivatives of $\boldsymbol{x}$; and $\boldsymbol{\delta}(t)$ is the unit impulse function. To achieve the desired frequency characteristics, the following mass and stiffness matrices were defined:

$$\boldsymbol{m} = m\boldsymbol{I} \quad \text{and} \quad \boldsymbol{k} = k\begin{bmatrix} 4 & -1 & 0 \\ -1 & 2 & -1 \\ 0 & -1 & 4 \end{bmatrix} \tag{A.2a,b}$$

where $\boldsymbol{I}$ is the identity matrix, $m = 1000$ kg and $k = 10$ kN/m. As the system is assumed to have a critical damping ratio $\xi = 0.01$ in each mode, a damping matrix can be defined as

$$\boldsymbol{c} = [\boldsymbol{m}\boldsymbol{\Phi}\boldsymbol{M}^{-1}]\begin{bmatrix} 2\xi\omega_1 M_1 & 0 & 0 \\ 0 & 2\xi\omega_2 M_2 & 0 \\ 0 & 0 & 2\xi\omega_3 M_3 \end{bmatrix}[\boldsymbol{M}^{-1}\boldsymbol{\Phi}^T\boldsymbol{m}] \tag{A.3}$$

where $M_{1,2,3}$ are the modal masses of the modal mass matrix $\boldsymbol{M}$, the modal frequencies are $\omega_{1,2,3} = 2\pi f_{1,2,3}$, and $\boldsymbol{\Phi}$ is the matrix of mode shapes. The response at the third degree of freedom of the MDOF system as the result of a unit impulse at that location was then generated via state-space simulation of Equation (19).